Strategies for Giant Mass-sensitivity using Super-high Frequency Acoustic Waves

Jian Zhou[a], Yanghui Liu[a], Zhengjia Zhan[a], Fengling Zhuo[a], Zhangbin Ji[a], Yuanjin Zheng[b], Yongqing Fu[c], Huigao Duan[a], *

Abstract—**Surface acoustic wave (SAW) devices are powerful platforms for mass sensing, chemical vapor or gas detection, and bio-molecular identification. Great efforts have been made to achieve high sensitivities by using super-high frequency SAW devices. Conventional SAW sensing is based on mass-loading effects at the acoustic wave propagation (or delay line) region between two interdigitated transducers (IDTs). However, for many super-high frequency SAW devices with their small sizes, there is a huge challenge that the sensitivity is difficult to be further increased, simply because there are very limited areas between the IDTs to deposit a sensing layer. Herein, we proposed a novel strategy based on giant mass-sensitivity effects generated on the global area of acoustic wave device (defined as areas of both delay line region and IDTs), which significantly enhances sensitivity and reduces detection limit of the SAW device. Both theoretical analysis and experimental results proved this new strategy and mechanism, which are mainly attributed to the efficient energy confinement at the IDTs region for the super-high frequency SAW devices. The achieved mass sensitivity using this new strategy is as high as 2590 MHz•mm^2•μg^{-1}, which is about 500 times higher than that obtained from only using the acoustic wave propagation region with a SAW frequency of 4.43 GHz. A hypersensitive humidity detection has been demonstrated using this newly proposed sensing platform, achieving an extremely high sensitivity of 278 kHz/%RH, fast response, and recovery times of ~37 s and~35s.**

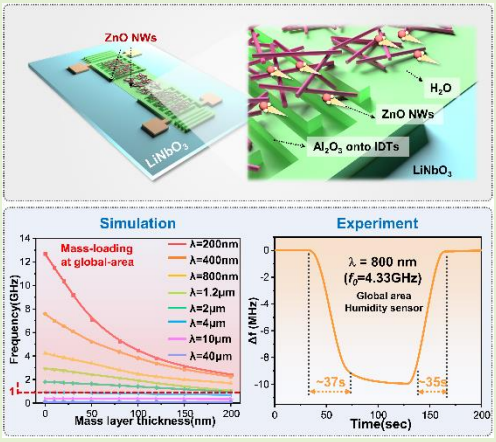

***Index Terms*—Ultrahigh frequency; SAW; global area; mass-loading effect; Hypersensitivity sensors**

I. Introduction

SURFACE acoustic wave (SAW) devices have been widely used as a sensing platform to monitor physical parameters, such as temperature, strain, mass, ultraviolet (UV) [1]-[4], or electrochemical and biological signals, including concentrations of ions, gas, molecules, protein and DNA [5]-[10]. For the SAW devices used for mass sensing, chemical vapor detection, and high precision bio-molecular identification, the sensing layer is normally deposited at the delay line region (or the acoustic wave propagation areas) between two opposite IDTs, which forms the fundamental sensing area as shown in Figures 1a&b. Mass-loading of particles, gas molecules, or bio-molecules at the acoustic wave propagation region will cause perturbation of the wave's velocity, leading to the shift of resonant frequencies [11]. SAW sensor's mass sensitivity can be calculated using equation $\Delta f = \frac{C f_0^2}{A}\Delta m$ [12], where A is the active surface area, C is a constant, Δf is the frequency shift, f_0 is the resonant frequency of the device, and Δm is the mass-loading or mass change.

To enhance the sensitivity of SAW devices using the mass-loading effect, a commonly used strategy is to increase the resonance frequency f_0. For example, Wohltjen et al. fabricated various SAW resonators with different resonance frequencies of 31, 52, 112, and 290 MHz, and confirmed that the mass sensitivity of SAW oscillators was increased with the frequency [13]. Dickert et al reported that the sensitivity of SAW-resonators was increased with the resonance frequencies increased from 80 MHz up to 1 GHz [14]. Cai et al measured the sensitivity of a SAW biosensor for DNA sequencing and cell detection, and obtained a high sensitivity of 6.7×10-16g/cm^2/Hz using the third-order harmonic mode of 6.4 GHz [15]. Since the resonance frequency of a SAW device is dependent on $f_0 = \frac{c}{\lambda}$ (where c is the acoustic wave velocity and λ is the SAW wavelength), it is needed to either increase the acoustic wave velocity or reduce the wavelength in order to further increase the frequency of the SAW sensor.

However, when the frequency of a SAW sensor is increased above GHz, there is a huge challenge to further reduce the

a. College of Mechanical and Vehicle Engineering, Hunan University, Changsha 410082, China
b. School of Electric and Electronical Engineering, Nanyang Technological University, 639798 Singapore
c. Faculty of Engineering and Environment, Northumbria University, Newcastle, NE1 8ST, United King-dom.

This work was supported by the Natural Science Foundation of China (NSFC No.52075162), the Program of High-tech Industry of Hunan Province (2020GK2015), The Natural Science Foundation of Hunan Province (2021JJ20018), Joint fund of the Ministry of Education (Young Talents), the Engineering Physics and Science Research Council of UK (EPSRC EP/P018998/1) and International Exchange Grant (IEC/NSFC/201078) through Royal Society and the NSFC.

distance between the opposite IDTs (often they are designed in sub-micrometer scales) As it is well-known, for these high-frequency SAW devices, if the distance between two IDTs is too large, there will be a significant propagation loss or deterioration of SAW transmission signals [12]. With such significantly reduced dimensions, There are not enough area and also it is difficult to deposit enough sensing layer in this region [16]. Therefore, it is highly desirable to explore an alternative strategy or a new sensing mechanism, which can overcome such limitations/contradictions and further push the detection limit for these super-high frequency SAW devices.

In 2020, our group proposed a new sensing mechanism which uses mass-loading effect directly on the IDT electrodes of SAW resonators [12]. This method enables enhanced sensitivity compared with that of the conventional SAW devices which are based on mass loading at the delay-line region. However, that proposed method using the IDT electrode sensing still has its limitations. For example, the metal IDT electrodes cannot be used in a liquid environment, or corrosive medium, and also conductive sensitive film cannot be used, as these will short-circuit or damage the IDTs. In addition, it also has a great challenge to deposit/fabricate sensing film directly onto the IDT electrodes, as these IDTs are often in nanoscales with GHz high frequencies. The self-assembly process of the sensing layer could be used to form sensing film onto IDTs, although is also difficult, but the other methods such as dip coating or spin coating are all unsuitable.

To address this issue, in this study, we propose a new strategy that integrates the mass-loading effects generated on a global area of the device (e.g., both the wave propagation area and two IDTs regions), thus achieving a super-high sensitivity for high-frequency SAW devices. Figure 1d shows our new concept to achieve such a giant mass-sensitivity effect based on the global area for high-frequency SAW devices. Theoretical analysis, simulations, and experimental results showed that the frequency shifts caused by mass loading in the global area are much larger than those of conventional sensing method which uses only the delay line region. We demonstrated that this enhancement becomes significant when the frequency of the SAW device is increased to above 1 GHz. The key mechanism of such an enhanced sensitivity was identified as the efficient energy confinement within the IDTs' area, which was theoretically investigated and experimentally verified. We further demonstrated its application for humidity sensing and obtained both super-high sensitivity and fast responses using this new sensing strategy.

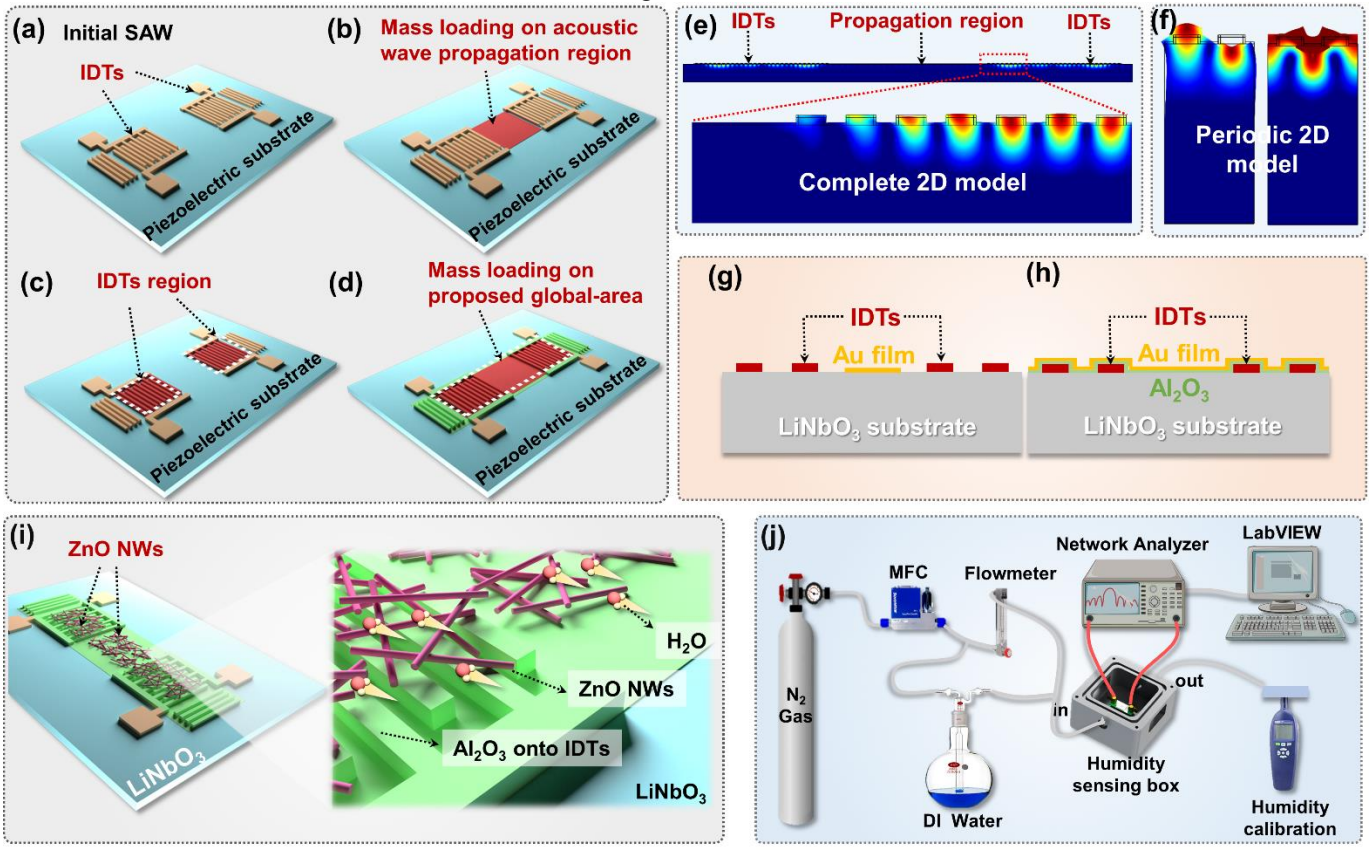

Figure 1. (a) SAW device that consists of IDTs and piezoelectric substrates; (b) SAW device with the conventional mass-loading region between two IDTs; (c) SAW device with the mass-loading region on the IDT electrodes; (d) The proposed new SAW device with the mass-loading region on the global area; (e) Complete 2D model of the SAW structure and its modal shapes; (f) 2D periodic model of the SAW structure and its modal shapes; (g) Schematic diagram of experiments of micro-mass using conventional sensing mechanism on propagation area; (h) A schematic diagram of experiments of micro-mass using proposed novel sensing mechanism on the global area; (i) A schematic illustration of SAW humidity sensor with the H_2O molecules adsorption mechanism on the proposed SAW sensitive layer; (j) A schematic view of the humidity SAW sensing testing system.

II. FEM Simulation and Theoretical Calculation

To compare the frequency shifts caused by the mass-loading effects based on the conventional acoustic wave propagation region and the newly proposed idea using the global area, a 2D model (using the COMSOL 5.4a) was established and analyzed

in the frequency domain of the global area (Figure 1e). In this model, the piezoelectric layer is $LiNbO_3$, the IDT electrode is Au with a thickness of 30 nm, and the wavelengths λ are 400 and 800 nm, respectively. For the mass loading effect of SAW devices in the acoustic propagation region, Au film is used as mass loading material. The thicknesses of Au film are 10 and 30 nm, and the mass loadings in the acoustic wave propagation area are ∼0.193 and ∼0.579 μg·mm^{-2}, respectively. To simulate the mass-loading effect from the global area on the frequency shift, an Al_2O_3 film is added onto the SAW global area surface with a thickness of 10 nm to act as an insulation layer. This layer can prevent the IDT electrodes to form a short circuit and protect the IDTs being damaged by the environment. The Au film was then added onto this insulation layer and the same mass-loading per unit area was applied, which can be compared with that of the case on the acoustic wave propagation area.

To investigate the sensing mechanisms and the main contributing factors of giant mass-loading effects on the global area of the SAW device, we have further simulated the frequency responses with the same mass-loading (0.386 μg·mm^{-2}) in three different cases, i.e., within the conventional propagation area, the IDT region, and the newly proposed global area at different wavelengths (i.e., from 400 nm to 20 μm). We also compared the frequency responses of mass-loading in the global area with those on the IDT region. The frequency-domain analysis using a completed 2D model and a periodic 2D model (Figure.1f) was conducted. The detailed simulation parameters are shown in the supporting information (SI).

Theoretical finite element model/boundary element model (i.e., FEM/BEM) were also applied for the verification of the simulation results. Green's function was employed for the semi-infinite piezoelectric material, and we only considered the charges at the electrode/substrate interfaces (z=0) [17]. The Green's function is described using the following equation:

$$\begin{pmatrix} u(x) \\ \varphi(x) \end{pmatrix} = \sum_{j=1}^{N_e} \int_{c_j-a_j}^{c_j+a_j} G_{\Upsilon}^{p}(x-x') \begin{pmatrix} t_s(x') \\ \sigma(x') \end{pmatrix} dx' \quad (1)$$

where φ is the electric potential, u is particle displacements, σ is the charges at the interface, t is the mechanical stress components in the z-direction, a_j is the half electrode width for the j^{th} electrode of the elementary period, c_j is the x coordinate of the electrode center, N_e is the number of electrodes for one period of the array, $G_{\Upsilon}^{P}(x)$ is the periodic harmonic Greens function (which was first introduced by Plessky et al [12]).

Next, the mechanical behavior of electrodes is simulated in the above system, where the electrodes are treated as being homogeneous, isotropic and elastic according to the method reported in Ref [18][19]. We have chosen to discretize each electrode into triangular elements. The FEA was performed using linear equations which show the relationship between nodal displacements and force vectors ($\boldsymbol{U}$, $\boldsymbol{F}$):

$$\left(\boldsymbol{K}-\omega^2\boldsymbol{M}\right)\boldsymbol{U}=\boldsymbol{F} \quad (2)$$

where $\boldsymbol{F}$ is computed from stresses $\boldsymbol{t}_s$, and $\boldsymbol{K}$, $\boldsymbol{M}$ are stiffness and mass matrix, respectively.

$$F_i = \int_{\Gamma_{es}} \boldsymbol{t}_s(x) W_i(x)\, dx \quad (3)$$

where $W_i(x)$ is the FEA basis function associated with node i [19].

The current which passes through the j^{th}-finger can be calculated using the following equation:

$$I_j = \int_{-a_j}^{a_j} \frac{\partial\sigma(x)}{\partial x} dx \quad (4)$$

Finally, we calculated the admittance matrix of the SAWs with arbitrary numbers of IDTs, and the frequency responses were obtained.

III. Experimental Section

We used the UV lithography process (See Figure S1) to fabricate low-frequency SAW devices (λ of 20 μm) and used electron beam lithography (EBL, See Figure S2) with a proximity effect correction (PEC) algorithm [1] to fabricate high frequency (λ of 800 nm) SAW devices, to verify the mass sensitivity at the global area of SAW devices. An optical microscope and a scanning electron microscope (SEM, model of Zeiss SIGMA HD) were used to characterize the SAW devices. For mass sensing in the propagation area or the delay line region, we directly deposited a 5 nm-thick Au film, which produced a mass loading of 0.0965 μg·mm^{-2} using a thermal evaporator (Figure 1g). For mass sensing based on the newly proposed global area of the SAW device, a 10 nm-thick Al_2O_3 insulating passivation film was firstly deposited using an atomic layer deposition (ALD) method to form an insulator layer onto the global-area of the device. Then, a 5 nm-thick Au film was deposited on the global area of the SAW device (Figure 1h). The detailed fabrication information is shown in SI. The S_{21} transmission spectra of the SAW devices were recorded before and after the deposition of such a mass loading layer, using a network analyzer (Ceyear 3656D).

We further demonstrated the humidity detection using the giant mass-sensitivity effect achieved from the global area of the SAW device. For this purpose, ZnO nanowires (NWs) were used as the sensing material (Figure 1i). A solution of ZnO NWs was dripped onto global areas (including the conventional acoustic wave propagation area and the global area), and then dried on a hot plate at 80 °C to form the sensitive layer of ZnO NWs. An SEM with its attached energy dispersive X-ray spectroscopy (EDS) was used to characterize the surface morphologies of the sensitive films. For humidity sensing, we used a wavelength of 20 μm for the low frequency SAWs and a wavelength of 800 nm for the high frequency SAW humidity sensor. The humidity testing system is shown in Figure 1j. N_2 (99.99% purity) was used as the carrier gas [20],[21]. Different relative humidity (RH) levels were achieved by precisely controlling the relative proportion of dry N_2 gas and wet N_2 gas, the latter of which was produced by passing dry N_2 through a bottle with the deionized water. The ratio of dry and wet gas flowing into the humidity box was controlled by adjusting the glass rotameter, in order to adjust the relative humidity. A mass flow meter (MFM) was used to ensure the total pressure unchanged during the experiments. A standard thermo-

hygrometer was used to calibrate the humidity level. The testing chamber's temperature was ~25°C. A LabVIEW program was applied to record the frequency changes as a function of time at different RH levels.

IV. RESULTS AND DISCUSSION

A. Mass-Loading Effects on Acoustic Wave Propagation Area and Global area of SAW device.

Figures 2a&b show the simulated shifts of the resonant frequencies due to the mass-loading effects, at the acoustic wave propagation area, and on the proposed global area of the SAW device with a wavelength of 400 nm, respectively.

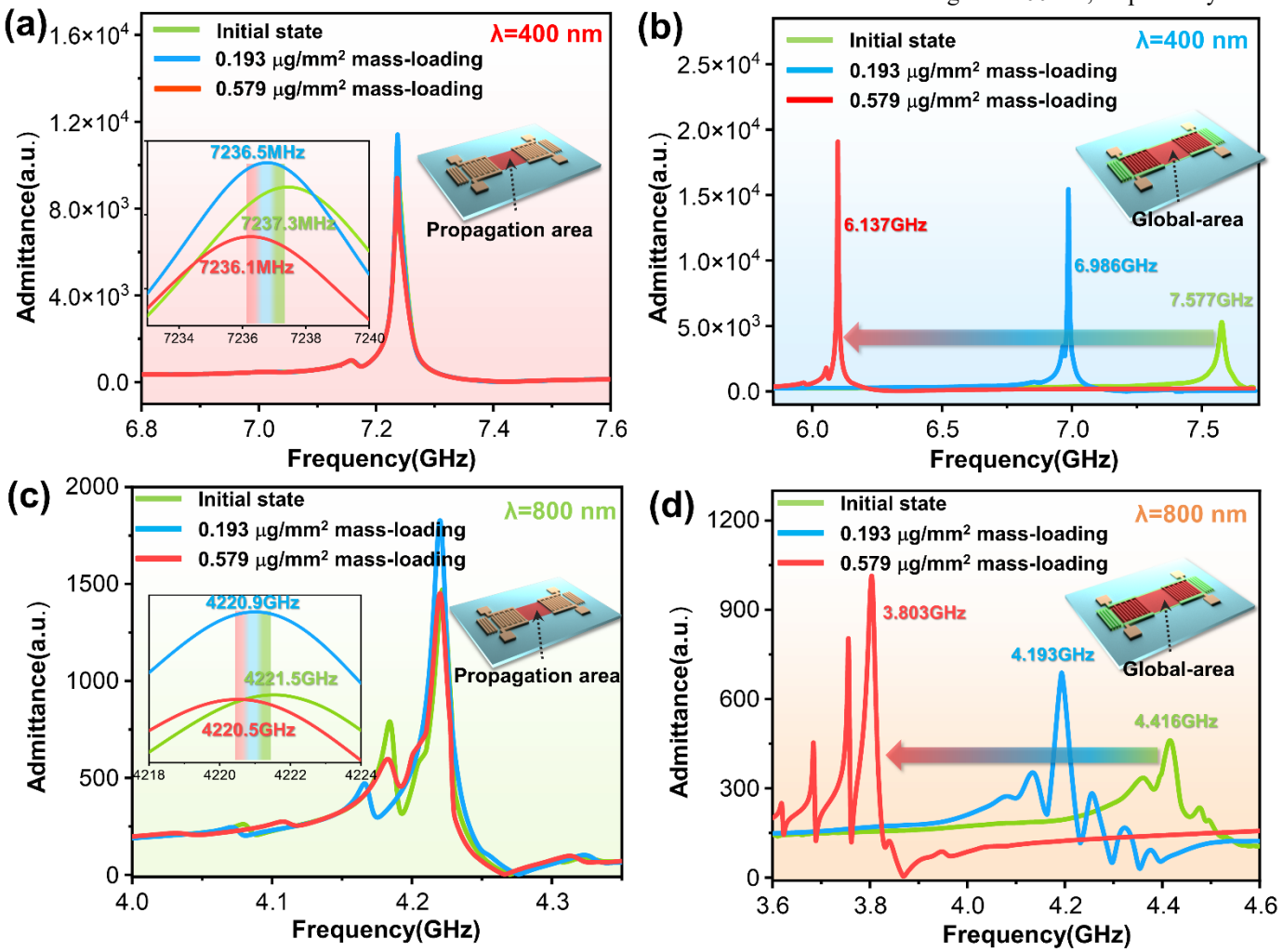

Figure 2. Simulated frequency responses of high frequency SAW devices with different mass loadings on (a) acoustic wave propagation are a between two IDTs with a wavelength of 400 nm; (b) global area with a wavelength of 400 nm; (c) acoustic wave propagation area with a wave-length of 800 nm; (d) global area with a wavelength of 800 nm.

As the mass-loading is increased from 0 to 0.193 and to 0.579 $\mu g \cdot mm^{-2}$ at the delay line region of the SAW device, the frequency is only shifted ~1.2 MHz, e.g., from 7.2373 to 7.2365, and then to 7.2361 GHz, respectively. Whereas for the mass-loading on the global area, the frequency is shifted up to ~1440 MHz, e.g., from 7.577 to 6.986, and then to 6.137 GHz. The results show that with the same mass-loading, the sensitivity based on the global area of the SAW device is 1200 times larger than that based on the delay line region. Similar results are obtained for the device with a wavelength of 800 nm as shown in Figures 2c&d. For the same mass loading, the frequency shifts are 1 MHz, and ~613 MHz, for the same mass loading on the delay line region and on the global area, respectively. These results reveal that the mass sensitivity obtained on the global area is significantly larger than those within the delay line region.

B. 4.2 Mechanism of Mass-Loading on global area of the SAW device.

To investigate the mechanisms and the contribution factors of giant mass-loading effects using the global area of SAW device for mass detection, we have simulated the frequency responses of SAWs with the same mass-loading (0.386 $\mu g \cdot mm^{-2}$) generated at the propagation area, the IDT region and the global area of the SAW device, respectively, at high-frequency range (λ of 400 and 800 nm), middle frequency range (λ of 3.2 and 4 μm), and low-frequency range (λ of 16 and 20 μm). Results in Figure 3 and **Table S1** show that the frequency shifts of SAW devices based on the global area are comparable to the sums of frequency shifts on the propagation area and the IDTs region for all the different wavelengths, demonstrating that a combination of mass-loadings on the propagation area and the IDTs region leads to mass-loading effects on the global

area.

Figure 3a shows that in the high frequency range with an IDT wavelength of 400 nm, the frequency shifts are about 7.4 MHz, 1036.6 MHz and 1036.7 MHz for the sensing layer at the wave propagation area, the IDTs region, and the global area, respectively. Figure 3b shows that for the wavelength of 800 nm, the shifts of the frequencies for the SAW devices are about 6.2 MHz, 405.2 MHz and 415.6 MHz for the sensing at the propagation area, the IDTs region and the global area, respectively. These results clearly show that, at high frequency range, the main contribution factor for the mass-loading effects at the global area giant of SAW devices is mainly contributed from the IDTs' region, whereas the mass-loading effect at propagation area is relatively insignificant.

In the middle frequency range (e.g., λ of 3.2 and 4 μm), results shown in Figures 3c&d still demonstrate a similar phenomenon, revealing that the main contribution factor for the frequency shifts is due to the mass-loading at the IDTs region. Whereas at the low frequency range (e.g., λ of 16 and 20 μm), we can observe that the frequency shifts of SAWs on global area are nearly in the same order of magnitude compared with those on the IDTs' region. The above results clearly demonstrate that the main contribution of giant mass-loading effects of SAW device is mainly from the IDTs area, especially for the high frequency SAW devices.

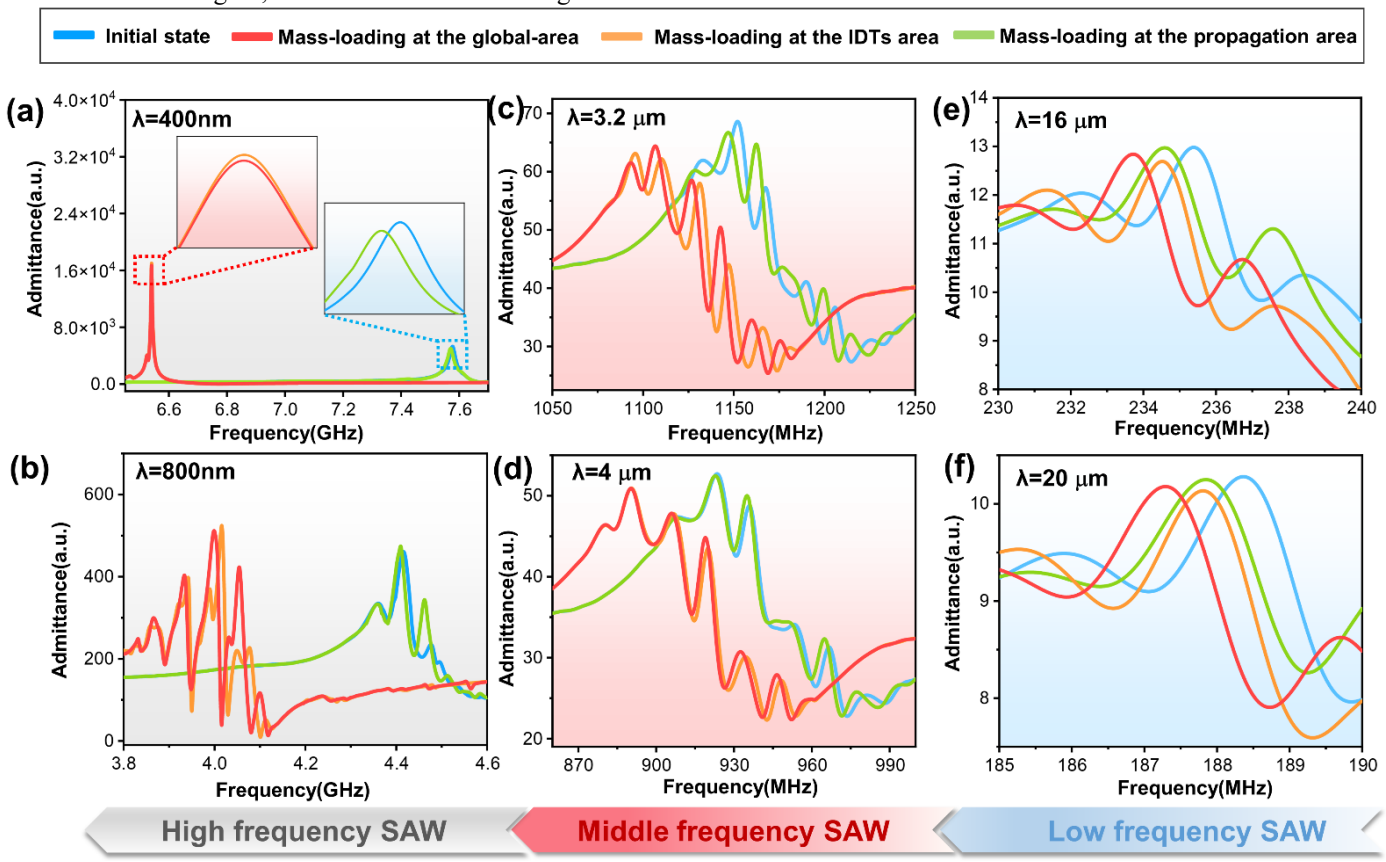

Figure 3. Simulated frequency responses for mass-loading effects at different areas (the wave propagation area, the IDTs region, and the global area) of a SAW device with a series of wave-lengths of (a) 400 nm; (b) 800 nm; (c) 3.2 μm; (d) 4 μm; (e) 16 μm; (f) 20 μm.

To further verify the main contribution of giant mass-sensitivity effect, different mass-loading simulations were performed on the $LiNbO_3$-based SAW devices with different wavelengths from 200 nm to 40 μm. Figures 4a&b show the mass-loading effects (e.g., with the increase of Au thicknesses from 10 nm to 90 nm) on both the global areas and IDT areas on the frequency responses with λ of 400 nm. The frequency shifts are similar for mass sensing at both the global areas and IDT areas with various mass-loading effects, verifying that the main contribution for this giant mass-sensitivity effect is from the mass-loading on the IDT areas. In addition, as the Au layer thickness is increased from 10 nm to 90 nm, the frequency is decreased by ~2.5 times, e.g., from 7.5 to 3 GHz at λ of 400 nm. However, with the λ value of 20 μm as shown in Figures 4c&d, the resonance frequency is only decreased by 5.2%, with the same mass-loading effect. These results confirm that the giant mass-loading effects are more significant at a higher frequency range. Figures 4e&f summarize the effects of different mass-loading effects at both the global areas and IDT areas for $LiNbO_3$-based SAW devices with wavelengths increased from 200 nm to 40 μm. The simulation results confirm that the main contribution for this giant mass-sensitivity effect is from the mass-loading on the IDT areas, and the mass loading on the global area has more significant effect on SAW frequency shifts when the SAW resonant frequency is larger than 1 GHz.

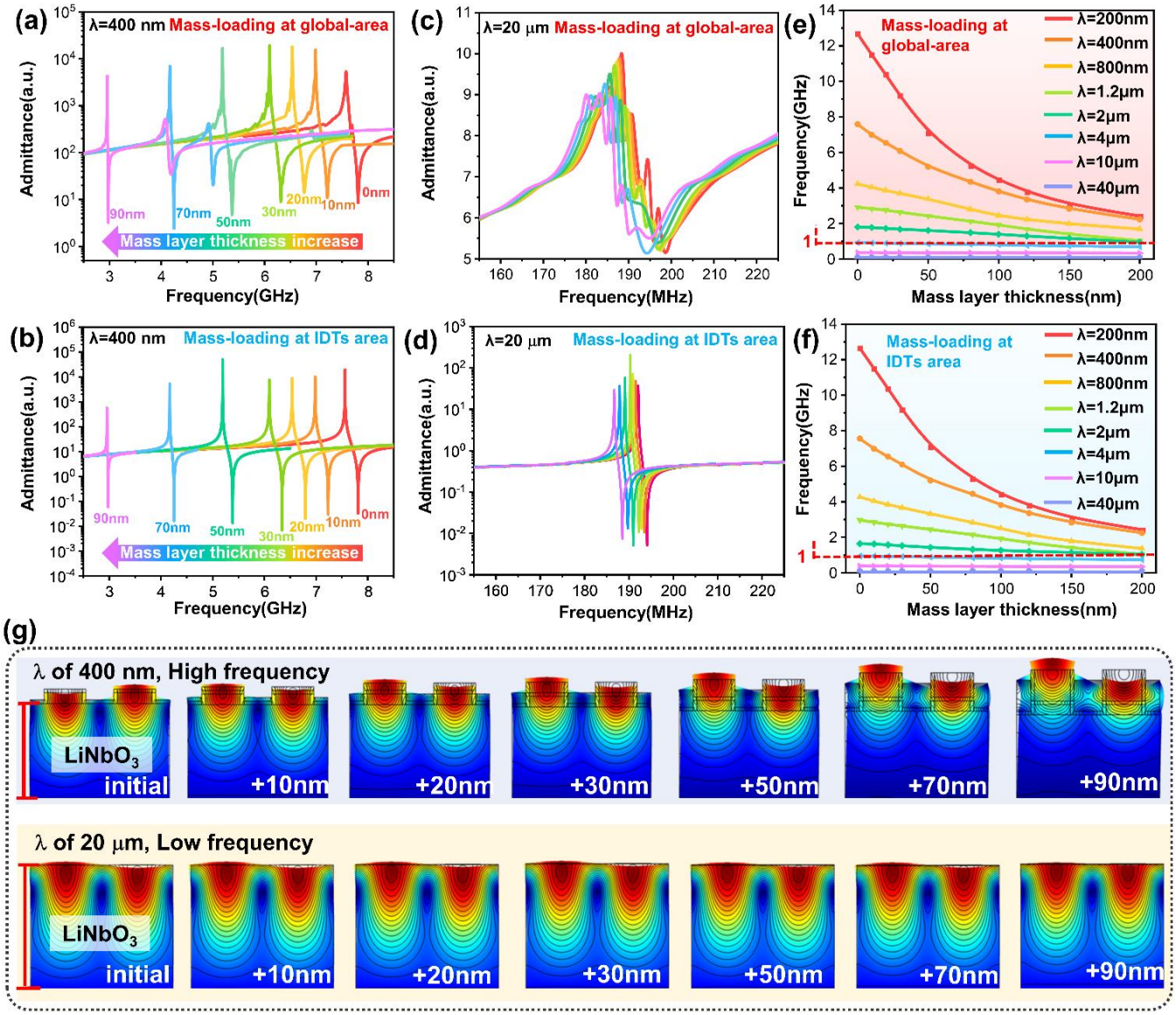

Figure 4. Simulated frequency response of different mass-loading (Au thickness from 10 nm to 90 nm) on: (a) Global area of SAW device with a λ of 400 nm; (b) IDT area of SAW with λ of 400 nm; (c) Global area of SAW device with a λ of 20 μm; (d) IDT area of SAW device with a λ of 20 μm; (e)&(f) Frequency shifts of different mass-loading on global area and IDT area, with a series of λ from 200 nm to 40 μm on the $LiNbO_3$; (g) The simulated vibration modes of the $LiNbO_3$-basd SAW sensor with different λ and Au thicknesses.

To understand the physical origins that the higher frequency leads to a significant mass-loading effect, we simulated the surface vibration patterns of the SAW devices with a mass-loading at IDT regions. The obtained results are shown in Figure 4g. For the SAW device with a relatively low frequency (e.g., λ of 20 μm), when the thickness of mass-loading of Au film is increased from 10 nm (0.5/1000 λ) to 90 nm (4.5/1000 λ), the changes of particle vibration modes and the IDT electrode shapes are insignificant. The surface vibration is mainly within the $LiNbO_3$ layer because the mass-loading thickness is much smaller than the microscale wavelength and the mass loading is a perturbation to the acoustic waves. However, for the super-high frequency SAW device with λ of 400 nm, there is a relatively large mass loading for high frequency SAW device but not the perturbation, when the Au layer thickness is increased from 10 nm (2.5/100 λ) to 90 nm (22.5/100 λ). Furthermore, the particle vibration patterns are changed significantly, e.g., being not concentrated much in the $LiNbO_3$ layer, but within the IDT regions. As the IDT region does not have piezoelectric effect, the wave velocity is significantly decreased.

As the IDT regions includes IDT fingers and IDT gaps, we further made different mass-loadings on IDT fingers using the $LiNbO_3$-based SAW devices with λ of 400 nm, and the obtained results are shown in **Figure S3**. The frequency shift is almost the same with the mass-loading on IDT regions, indicating that the giant mass-loading effects are originated from the mass-loading at IDTs electrodes. Furthermore, the particle's vibration patterns (**Figure S4**) confirm that the acoustic energy being confined into electrodes leads to a significant decrease of the wave velocity. We have further performed calculations of frequency changes using FEM/BEM for the SAW device with a λ of 400 nm. The obtained results are shown in **Figure S5**, from which a similar trend of frequency changes with those from the simulation is obtained, demonstrating the reliability of the simulated results.

C. Experimental Demonstration of Giant Mass-Loading Effects at Global area of SAW device.

We performed the mass sensing tests to verify the giant mass-sensitivity effect at the global areas of the SAW devices. The fabricated SAW devices with a low frequency (λ of 20 μm) and a high frequency (λ of 800 nm) are shown in Figures 5a&b, which demonstrate the high quality of the fabricated IDTs. For the sensing based on the wave propagation area, a 5 nm-thick Au film (corresponding to a mass loading of 0.0965 μg·mm^{-2}) was deposited at both propagation area (Figures 5c&d) and the global area (Figures 5e&f). The detailed device parameters and properties are listed in **Table S2**.

Figures 5g&h present the frequency shifts of low frequency SAW devices (λ of 20 μm) with the same mass-loading, on the acoustic wave propagation area and the global area, respectively. The obtained results show that the frequency shift caused by mass loading of surface acoustic wave devices in the acoustic propagation region is about 0.25 MHz, whereas the frequency shift due to the mass loading at the global area is 0.5 MHz, which is doubled. These results clearly show that at a low frequency range, the mass-loading on the global area is slightly more sensitive than that on the acoustic wave propagation area.

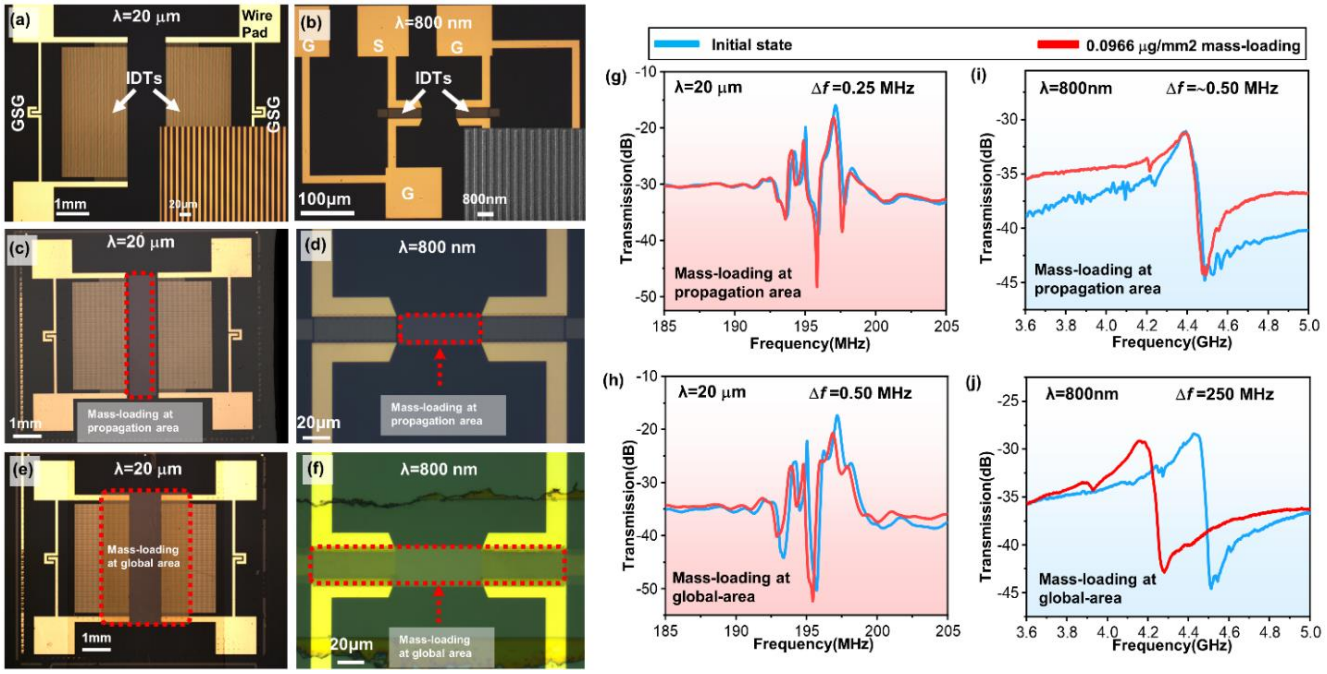

Figure 5. Optical image of the fabricated low-frequency SAW device with λ of 20 μm for (a) initial state; (c) 5 nm-thick Au film at the propagation area;(e) 5nm-thick Au film at the global area. Optical image of the fabricated high-frequency SAW device with λ of 800 nm for (b) initial state; (d) 5nm-thick Au film at the propagation area; (f) 5nm-thick Au film at the global area. Experimental mass-sensor results of the frequency response of SAW devices. (g) Mass loading on propagation area of SAW with a wavelength of 20 μm; (h) Mass loading on global area of SAW with a wavelength of 20 μm; (i) Mass loading on propagation area of SAW with a wavelength of 800 nm; (j) Mass loading on global area of SAW with a wavelength of 800 nm.

However, for the cases of the devices with much higher frequency (e.g., λ of 800 nm), results are significantly different. As shown in Figures 5i&j, under the same mass-loading of 0.0965 μg·mm^{-2}, the frequency shift of the SAW device due to the mass loading at the acoustic wave propagation area is only about 0.5 MHz, whereas the frequency shift at the global area of the SAW device is about 250 MHz for the SAW sensor with the wavelength of 800 nm. The corresponding mass sensitivity at global area is 2590 MHz•mm^2•μg^{-1}, which is 500 times larger than that at acoustic wave propagation area (5.2 MHz•mm^2•μg^{-1}) for the SAW frequency of 4.43 GHz.

In addition, when the resonance frequency is increased from 197 MHz to 4.43 GHz, the frequency shift is only increased from 0.25 MHz to 0.5 MHz for the acoustic wave propagation area (Figures 5g&i). Whereas the frequency shift is increased from 0.5 MHz to 250 MHz for the mass-loading at global area (Figures 5h&j). These experimental results verified that the proposed sensing method based on the global area is more suitable for ultrahigh frequency SAW devices.

D. Giant Mass-Loading Effects Used for Hypersensitive Humidity Sensing.

Figure 6a shows an SEM image of the fabricated high-frequency (λ of 800 nm) SAW sensor deposited with ZnO NWs. The ZnO NWs were decorated at the surface of the global area of SAW device, and their porous structures provide numerous absorption sites for water molecules. Figures 6b&c show the EDS elemental mapping of the ZnO NWs, revealing that the ZnO NWs were successfully deposited onto the global area of the SAW device.

Figure 6d shows variations of the resonant frequencies of a low frequency (λ=20 μm, 198 MHz) SAW device based on the propagation area and the global area, and also those of a high frequency (λ=800 nm, 4.33 GHz) SAW device based on the global area. The relative humidity was changed from 10% to 70% for five cycles. The resonance frequency was decreased when the RH level was increased from 10% to 70% due to the adsorption of water molecules, and the frequency was returned to the original value when the humidity was decreased from 70% to 10%, without any apparent saturation. The results demonstrate good repeatability and stability from 10% to 70%,

for both the acoustic wave propagation area and the global area of the SAW device. The low-frequency sensor based on the propagation area achieved a maximum frequency shift of 7.5 kHz, whereas the low-frequency sensor based on the global area achieved a nearly doubled frequency shift of 15 kHz. This result is consistent with those from the previous mass sensing and simulation results. Whereas for the high-frequency SAW sensor, a frequency shift of 10 MHz was achieved as the relative humidity is increased from 10% to 70%, which is more than 1333 times improvement compared with the low-frequency SAW humidity sensor.

Figure 6e summarizes the variations of resonance frequencies at different RH levels (10% ~ 85%) of the SAW sensor based on the global area. In general, the resonance frequencies of the SAW sensors show a nonlinear or exponential relationship to the humidity, similar to those reported in the literature [22]. Therefore, a log function between the frequency shift and relative humidity changes can be described using the following relationship

$$ln\,\Delta f = a(RH - RH_0) + b \quad (5)$$

where Δf is the shift of resonant frequency, RH_0 is the reference relative humidity, a and b are two coefficient constants. The ln Δf has a linear relationship with the RH levels ($R^2 = 0.948$) for the high-frequency SAW sensor at the global area, as shown in Figure 6f.

The sensitivity (S) of a humidity sensor is defined as:

$$S = \frac{|\Delta f|}{\Delta RH} \quad (6)$$

where Δf and ΔRH are the frequency shifts and humidity changes, respectively. The calculated average humidity sensitivity of the measured high-frequency SAW sensor is as large as 278 kHz/%RH within the humidity range of 10~85% RH, which is much higher than those of the other reported SAW-based humidity sensors, as listed in Table 2. The highest humidity sensitivity is 1.23 MHz/%RH, at the humidity point of 85% RH.

Figures 6g&h show the response and recovery times of high frequency SAW humidity sensors. The corresponding response time and recovery time are about 37 s and 35 s, respectively, which are much shorter than those of low frequency SAW for both acoustic wave propagation area and the global area of the SAW device. Results showed that sensing based on the global area at a higher frequency can greatly reduce the response time and recovery time of the SAW humidity sensors.

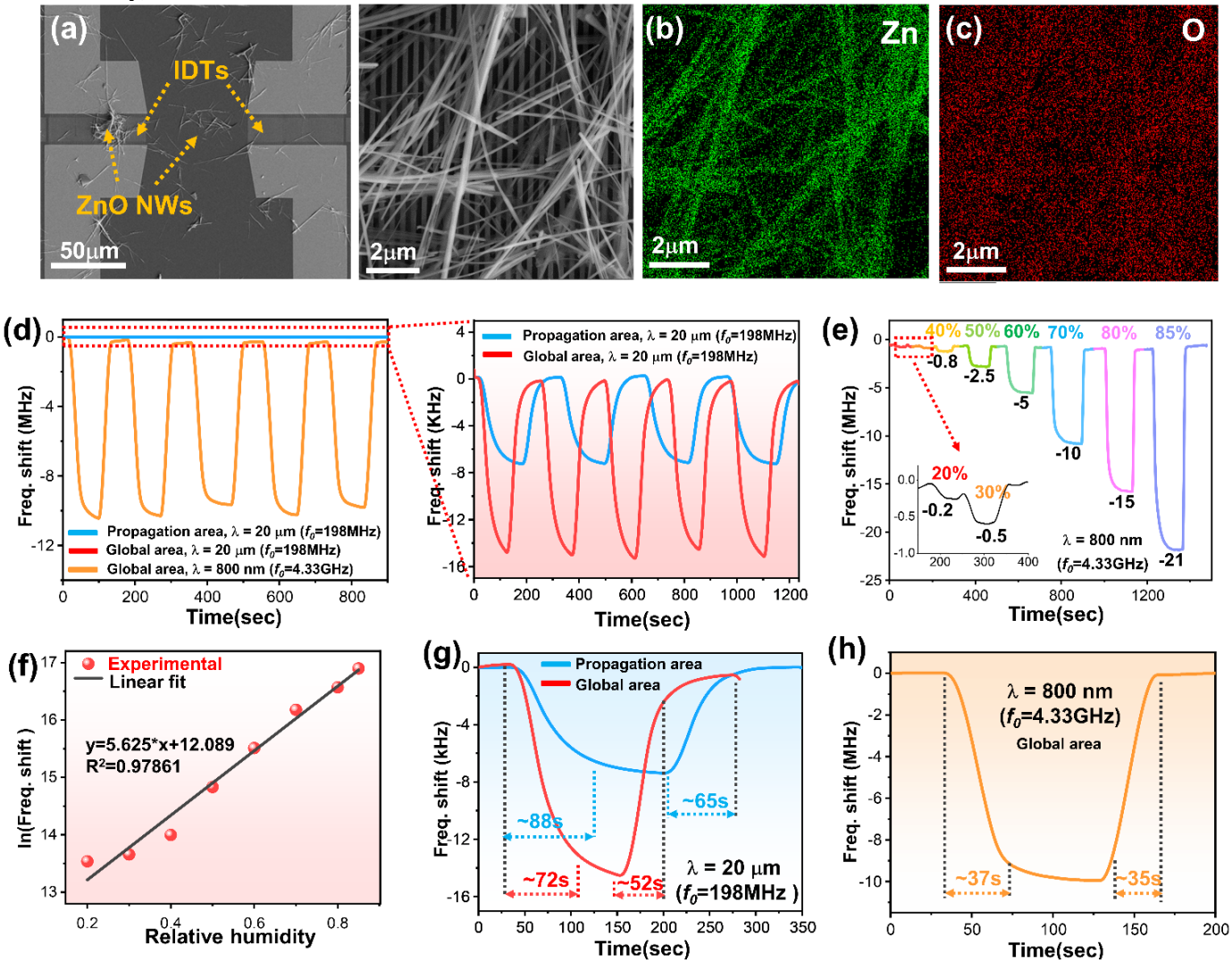

Figure 6. (a) SEM image of high-frequency SAW humidity sensor with ZnO NWs; (b)&(c) EDS elemental mapping of Zn and O elements of high-frequency SAW sensor; (d) Frequency comparison of SAW humidity sensors with sensing mechanism on both propagation area and global area for low-frequency SAW,

and on global area for high-frequency SAW, with the humidity changed from 10 to 70% RH for several cycles. (e) Dynamic responses of the high-frequency SAW sensors based on global area sensing toward the humidity changed from 10 to 85% RH; (f) The experimental and linearly fitted response curves toward the humidity at various RH for high frequency SAW based on global area. (g) Response and recovery time of low frequency SAW humidity sensors based on propagation area and global area, with the humidity level changed from 10 to 70% RH; (h) Response and recovery time of high frequency SAW humidity sensors based on global area, with the humidity level changed from 10 to 70% RH.

Table 2. Comparisons of sensitivities of different SAW-based humidity sensors

Ref.	*Year*	*f [MHz]*	*Sensing material*	*Sensitivity [KHz/% RH]*	*Measuring range*	*Resp./Rec. time*
[23]	2015	199.3	sol-gel method SiO_2	8.25kHz/%RH	30%~93%	12s/5s
[24]	2015	300.4	ZnO layer	7.1kHZ/%RH	5%~95%	N/A
[25]	2016	1.56GHz	CeO_2 NPs /PVP nanofibers	29.76kHz/%RH	11%~95%	20s/25s
[26]	2018	392	GO	42.08kHz(@80%RH)	10%~90%	22s/8s
[27]	2018	222	GO	91kHz/%RH	3.6%~98%	600s/6s
[28]	2019	226.3	GO	25.3kHz/%RH	10%~90%	10s/9s
[8]	2020	204.3	(3DAG)/PVA/SiO_2	2.429kHz(55%-90%RH)	0%~90%	24s/14.4s
[5]	2020	219.6	ZnO NW/GQD	40.16kHz/%RH	30%~80%	27s/12s
This work	**2022**	**4.33GHz**	**ZnO NW**	**278kHz/%RH**	**10%~85%**	**37/35s**

V. Conclusion

In this work, a new sensing strategy was proposed, based on the giant mass-sensitivity effect achieved on a global area of the SAW device. The sensitivity of the device has thus been significantly increased compared with those from the conventional sensing mechanisms. The enhanced mechanism for the sensitivity based on the global area of the SAW device is attributed to the giant mass-loading effect, which has been theoretically investigated and experimentally verified in this study. The achieved mass sensitivity at the global area of the SAW device is 2590 $MHz \cdot mm^2 \cdot \mu g^{-1}$, which is 500 times larger than that at conventional acoustic wave propagation area for the high frequency (4.43 GHz) SAW device. Based on this novel concept, we demonstrated for a humidity detection application, and obtained an extremely high sensitivity of 278 kHz/%RH, with a fast response and recovery time of about 37 and 35 s. This work opens new vistas for the development of a super high-frequency SAW platform for micro-mass sensing, trace chemical vapor detection and bio-molecular identification.

References

[1] Zheng, J.; Zhou, J.; Zeng, P.; Liu, Y.; Shen, Y.; et al., "30 GHz surface acoustic wave transducers with extremely high mass sensitivity," Appl. Phys. Lett., 2020, 116, 123502.

[2] Ji, Z.; Zhou, J.; Lin, H.; Wu, J.; Zhang, D.; et al., "Flexible thin-film acoustic wave devices with off-axis bending characteristics for multisensing applications," Microsyst. Nanoeng., 2021, 7, 97.

[3] Okuda, S.; Ono, T.; Kanai, Y.; Ikuta, T.; Shimatani, M.; et al., "Matsumoto, K. Graphene Surface Acoustic Wave Sensor for Simultaneous Detection of Charge and Mass," ACS Sens., 2018, 3 (1), 200-204.

[4] Weng, H.; Duan, F. L.; Xie, Z.; Liu, S.; Ji, Z., "LiNbO3-Based SAW Sensors Capable to Measure up to 1100°C High Temperature," IEEE Sens.J., 2020, 20 (21), 12679-12683.

[5] Wu, J.; Yin, C.; Zhou, J.; Li, H.; Liu, Y.; et al., "Ultrathin Glass-Based Flexible, Transparent, and Ultrasensitive Surface Acoustic Wave Humidity Sensor with ZnO Nanowires and Graphene Quantum Dots," ACS Appl. Mater. Interfaces, 2020, 12 (35), 39817-39825.

[6] Xiong, S.; Zhou, J.; Wu, J.; Li, H.; Duan, H; et al., "High Performance Acoustic Wave Nitro-gen Dioxide Sensor with Ultraviolet Activated 3D Porous Architecture of Ag-Decorated Reduced Graphene Oxide and Polypyrrole Aerogel," ACS Appl. Mater. Interfaces, 2021, 13 (35), 42094-42103.

[7] Agostini, M.; Amato, F.; Vieri, M. L.; Greco, G.; Tonazzini, I.; et al., "Glial-fibrillary-acidic-protein (GFAP) biomarker detection in serum-matrix: Functionalization strategies and detection by an ultra-high-frequency surface-acoustic-wave (UHF-SAW) lab-on-chip," Biosens Bioelectron, 2021, 172, 112774.

[8] Su, Y.; Li, C.; Li, M.; Li, H.; Xu, S., "Surface acoustic wave humidity sensor based on three-dimensional architecture graphene/PVA/SiO2 and its application for respiration monitoring," Sens. Actuators, B, 2020, 308, 127693.

[9] Tsougeni, K.; Kaprou, G.; Loukas, C. M.; Papadakis, G.; Hamiot, A.; et al., "Lab-on-Chip platform and protocol for rapid foodborne pathogen detection comprising on-chip cell capture, lysis, DNA amplification and surface-acoustic-wave detection," Sens. Actuators, B, 2020, 320, 128345.

[10] Wang, C.; Wang, C.; Jin, D.; Yu, Y.; Yang, F.; et al., "AuNP-Amplified Surface Acoustic Wave Sensor for the Quantification of Exosomes," ACS Sens., 2020, 5 (2), 362-369.

[11] McGinn, C. K.; Lamport, Z. A.; Kymissis, I, "Review of Gravimetric Sensing of Volatile Organic Compounds," ACS Sens., 2020, 5 (6), 1514-1534.

[12] Chen, Z.; Zhou, J.; Tang, H.; Liu, Y.; Shen, Y. P.; et al, "Ultrahigh-Frequency Surface Acoustic Wave Sensors with Giant Mass-Loading Effects on Electrodes," Acs Sens., 2020, 5 (6), 1657-1664.

[13] Wohltjen, H.; Snow, A. W.; Barger, W. R.; Ballantine, D. S., "Trace chemical vapor detection using SAW delay line oscillators," IEEE transactions on ultrasonics, ferroelectrics, and frequency control, 1987, 34 (2), 172-178.

[14] Dickert, F. L.; Forth, P.; Bulst, W.-E.; Fischerauer, G.; Knauer, U, "SAW devices-sensitivity enhancement in going from 80 MHz to 1 GHz," Sens. Actuators, B, 1998, 46 (2), 120-125.

[15] Cai, H. L.; Yang, Y.; Chen, X.; Mohammad, M. A.; Ye, T. X.; et al., "A third-order mode high frequency biosensor with atomic resolution," Biosens Bioelectron, 2015, 71, 261-268.

[16] Agostini, M.; Greco, G.; Cecchini, M. A, "Rayleigh surface acoustic wave (R-SAW) resonator biosensor based on positive and negative reflectors with sub-nanomolar limit of detection," Sens. Actuators, B, 2018, 254, 1-7.

[17] Ventura, P.; Hode, J. M.; Lopes, B., "Rigorous analysis of finite SAW devices with arbitrary electrode geometries, "In 1995 IEEE Ultrasonics Symposium. Proceedings. An International Symposium, Seattle. WA. USA, Nov, 1995; IEEE: Vol. 1 pp 257-262.

[18] Plessky, V. P.; Thorvaldsson, T., "Periodic Green's function analysis of SAW and leaky SAW propagation in a periodic system of electrodes on a piezoelectric crystal," IEEE Transactions on Ultrasonics Ferroelectrics & Frequency Control, 1995, 42 (2), 280-293.

[19] Zhou, J.; Shi, X.; Xiao, D.; Wu, X.; Zheng, J.; et al., "Surface acoustic wave devices with graphene interdigitated transducers," J. Mater. Chem. C, 2019, 29, 1.
[20] Mohamed Safian, N.; Anuar, A.; Omar, A.; Bawazeer, T.; et al., "Enhanced sensitivity of zinc phthalocyanine-based microporous humidity sensors by varying size of electrode gaps," Sens. Actuators, B, 2021, 343, 130158.
[21] Wang, Q.; Tong, J.; Wang, N.; Chen, S.; et al., "Humidity sensor of tunnel-cracked nick-el@polyurethane sponge for respiratory and perspiration sensing," Sens. Actuators, B, 2021, 330, 129322.
[22] He, X. L.; Li, D. J.; Zhou, J.; Wang, W. B.; Xuan, W. P.; et al., "High sensitivity humidity sensors using flexible surface acoustic wave devices made on nanocrystalline ZnO/polyimide substrates," J. Mater. Chem. C 2013, 1, 39.
[23] Tang, Y.; Li, Z.; Ma, J.; Wang, L.; Yang, J.; et al., "Highly sensitive surface acoustic wave (SAW) humidity sensors based on sol–gel SiO2 films: Investigations on the sensing property and mechanism," Sens. Actuators, B, 2015, 215, 283-291.
[24] Lan, X.-d.; Zhang, S.-y.; Wang, Y.; Fan, L.; Shui, X.-j., "Humidity responses of Love wave sensors based on ZnO/R-sapphire bilayer structures," Sens. Actuators, A, 2015, 230, 136-141.
[25] Liu, Y.; Huang, H.; Wang, L.; Cai, D.; Liu, B.; et al., "Electrospun CeO 2 nanoparticles/PVP nanofibers based high-frequency surface acoustic wave humidity sensor," Sens. Actuators, B, 2016, 223, 730-737.
[26] Le, X.; Wang, X.; Pang, J.; Liu, Y.; Fang, B.; et al., "A high performance humidity sensor based on surface acoustic wave and graphene oxide on AlN/Si layered structure," Sens. Actuators, B, 2018, 255, 2454-2461.
[27] Kuznetsova, I. E.; Anisimkin, V. I.; Kolesov, V. V.; Kashin, V. V.; Osipenko, V. A.; et al., "Sezawa wave acoustic humidity sensor based on graphene oxide sensitive film with enhanced sensitivity," Sens. Actuators, B, 2018, 272, 236-242.
[28] Le, X.; Liu, Y.; Peng, L.; Pang, J.; Xu, Z.; et al., "Surface acoustic wave humidity sensors based on uniform and thickness controllable graphene oxide thin films formed by surface tension," Microsyst. Nanoeng., 2019, 5, 36.

Jian Zhou received his Ph.D. (2015) in Electronic Science and technology from Zhejiang University (China). Currently, He is an associate Professor in College of Mechanical and Vehicle Engineering at Hunan University. His current research interests focus on MEMS sensors, SAW devices, flexible electronics devices and their advanced applications. Up to now, He has published more than 70 academic papers.

Yanghui Liu is currently a master student in College of Mechanical and Vehicle Engineering at Hunan University. He received his B.S. degree (2020) in School of Mechanical Engineering from Nanjing University of Science and Technology. His research focuses on the super-high frequency SAW devices, gas sensors, and advanced manufacturing.

Zhengjia Zhan received the B.S. (2019) and M.S. (2022) in College of Mechanical and Vehicle Engineering, Hunan University. His research interests include SAW devices, sensing mechanism, micro mass sensors.

Fengling Zhuo is currently a master student in College of Mechanical and Vehicle Engineering at Hunan University. She received her B.S. (2020) from Harbin University of Science and Technology. Her current research interests include the hydrogel bioelectronics and their advanced applications in multifunctional wearable electronic devices.

Zhangbin Ji is currently a master student in College of Mechanical and Vehicle Engineering at Hunan University. He received his B.S. (2020) from North University of China. His research mainly focuses on SAW devices, elastic mechanics, and strain sensors.

Yuanjin Zheng received his B.Eng. (1993) and M.Eng.(1996) from Xi'an Jiaotong University, Xi'an, China, and Ph.D. (2011) from Nanyang Technological University, Singapore. His current research interests include gigahertz radio frequency integrated circuit and SoC design, biosensors and imaging, and surface acoustic wave/bulk acoustic wave/microelectromechanical systems sensors.

Richard (Yongqing) Fu received his Ph.D. (1999) from Nanyang Technological University, Singapore, and then worked as a Research Fellow in Singapore-Massachusetts Institute of Technology Alliance, Singapore, and a Research Associate in University of Cambridge, Cambridge. He was a Lecturer with Heriot-Watt University, Edinburgh, UK, and then a Reader in Thin Film Centre, University of West of Scotland, Glasgow, UK, before moving to Newcastle, UK. He has extensive experience in smart thin films/materials, biomedical microdevices, energy materials, lab-on-chip, micromechanics, MEMS, nanotechnology, sensors, and microfluidics. He published over 450 science citation index (SCI) journal papers with current Google Scholar H-index of 70 with over 22,000 citations.

Huigao Duan received his B.S. (2004) and Ph.D. (2010) in Physics from Lanzhou University, China. He is currently a Professor in College of Mechanical and Vehicle Engineering, and a member of the State Key Laboratory of Advanced Design and Manufacturing for Vehicle Body, Hunan University, China. His current research interests include sub-10 nm patterning, nanophotonics, smart micro/nanosystems and their relevant applications.